ACS OMEGA

http://pubs.acs.org/journal/acsodf

Article

Quantitative Prediction of Charge Mobilities and Theoretical Insight into the Regulation of Site-Specific Trifluoromethylethynyl Substitution to Electronic and Charge Transport Properties of 9,10-Anthraquinone

Jin-Dou Huang and Huipeng Ma*

Cite This: *ACS Omega* 2022, 7, 48391−48402

Read Online

ACCESS | Metrics & More | Article Recommendations | Supporting Information

ABSTRACT: Herein, we systematically studied the electronic and conducting properties of 9,10-anthraquinone (**AQ**) and its derivatives and discussed the substitute-site effects on their organic field-effect transistor (OFET) properties in detail. Our calculation results show the influence of different substitute sites on the ionization potential (IP), electronic affinity (EA), reorganization energy (λ), electronic couplings (V), and anisotropic mobility (μ) of semiconducting materials, which mainly originates from the variations of the frontier molecular orbital charge distributions, the steric hindrance, and the conjugate degree. Combining quantum-chemical calculations with charge transfer theory, we simulated the intermolecular hopping rate in the organic crystals of **AQ** derivatives and predicted the fluctuation range of three-dimensional (3D) anisotropic charge carrier mobility for the first time. Our calculation results well reproduced the experimental observations and provided evidence for the determination of the optimal OFET conduction plane and channel direction relative to the crystal axis.

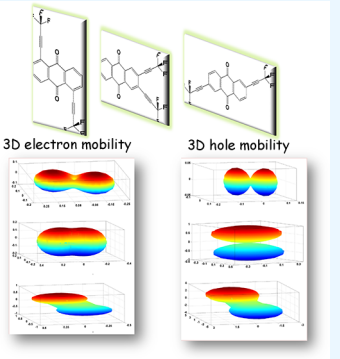

1. INTRODUCTION

Organic semiconductor materials play a significant role in various fields such as bioelectronics,[1,2] organic solar cells,[3−5] optoelectronic devices,[6,7] and biological sensors.[8,9] In the past decade, considerable attention was devoted to n-type semiconductors because of their wide-ranging applications in electronic devices, such as n-channel organic field-effect transistors (OFETs) and organic light-emitting diodes (OLEDs).[1−3] Nevertheless, the development of n-type semiconductors has largely lagged behind that of the p-type counterparts, which has limited the development of practical organic electronics.[6,10] The principal challenges for the n-channel semiconductors are their ambient instability and low electron mobility. Recently, some strategies have been introduced to optimize the electron transport layer for better ambient stability, such as lowering frontier molecular orbital (FMO) energies or introducing kinetic O_2/H_2O barriers.[6] A typical example of stable n-channel semiconductors is rylene diimide, which is designed by a LUMO regulation strategy. As a result of the substitution of an aromatic core with two sets of π-accepting imides groups, rylene diimide and its derivatives exhibit an electron-deficient nature and relatively low LUMO energies (high electron affinities) and have been widely used as building blocks for electronic devices.[3,6,10] Aside from chemically synthesizing new electron-deficient π-building blocks, appropriate regulation of the existing materials with electron-withdrawing groups is also an environmental-friendly and cost-effective way to achieve excellent properties, such as high field effect mobility and robust environmental stability. For example, Usta et al. designed and synthesized the first example of a benzothienobenzothiopene (BTBT)-based n-type molecular semiconductor via a symmetric functionalization of the BTBT π-core with pentafluorophenylcarbonyl groups, and the corresponding TC/BG-OFET devices demonstrated high electron mobilities of up to 0.6 $cm^2 \cdot V^{-1} \cdot s^{-1}$.[11] Zhao et al. put forth a new design of n-type organic semiconductors, which has trifluoromenthyethynyl groups attached to 9,10-anthraquinone (**AQ**) at different positions, and most of these trifluoromethylated anthraquinones behaved as n-type semiconductors in solution-processed FETs with electron mobilities of up to 0.28 $cm^2 \cdot V^{-1} \cdot s^{-1}$.[12] Limited to experimental testing methods, the influencing mechanism of molecular modification on the charge transport properties and ambient stability of organic semiconducting materials remains controversial and is urgently needed to be explored theoretically.

On the other hand, the determination of the intrinsic carrier mobility that reflects the conductive capacity of the charge carrier in ideal single-crystal structures is still a challenge to the present experimental methods. As one of the most important

Received: October 12, 2022
Accepted: December 5, 2022
Published: December 14, 2022

https://doi.org/10.1021/acsomega.2c06591
ACS Omega 2022, 7, 48391−48402

Scheme 1. Molecular Structures of 9,10-Anthraquinone (AQ) and Its Derivatives AQ12, AQ13, AQ14, AQ15, AQ17, AQ18, AQ23, AQ26, AQ27, AQ38, AQ1458, and AQ2356

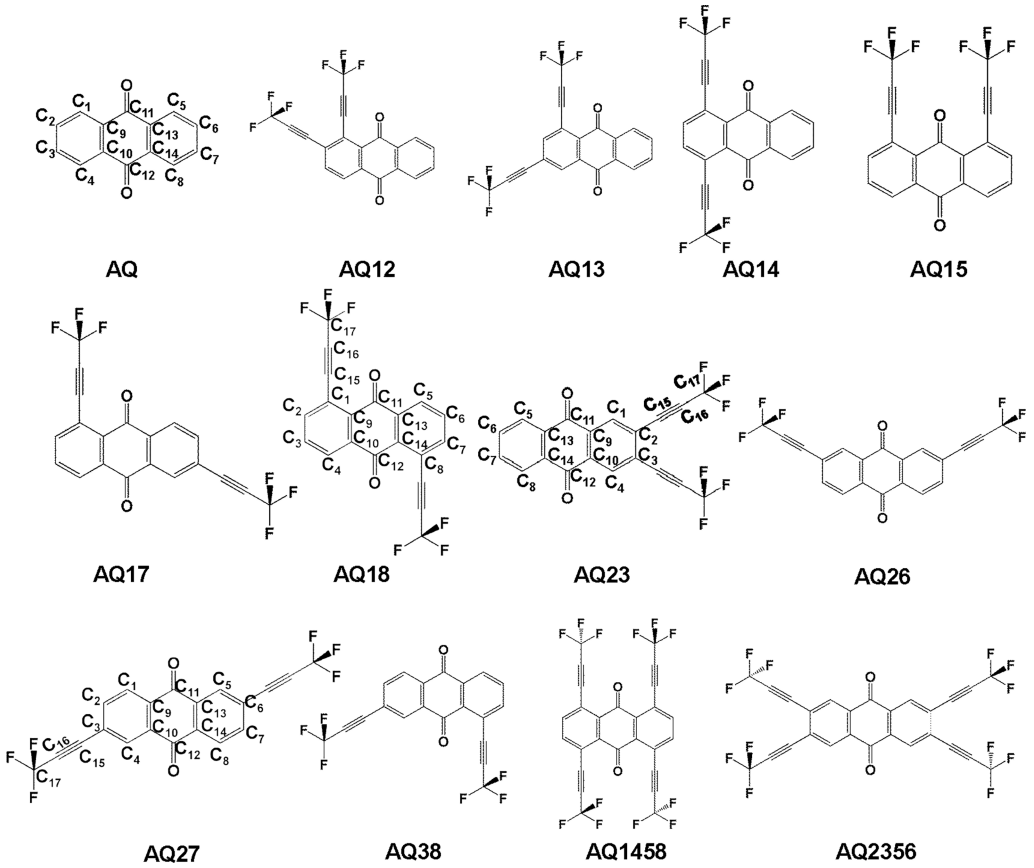

physical properties, the intrinsic anisotropic charge carrier mobility provides reference for the optimization of field-effect mobility in organic electronic devices, and its value depends mainly on the molecular properties and molecular packing modes in theory; however, the experimental results of mobility are also affected by experimental conditions, such as measurement methods, microstructural characteristics of the dielectric layers, the semiconductor film-deposition temperature, and so on,[13] and thus, the direct determination of the intrinsic carrier mobility through a theoretical simulation method is an important and necessary task. Since the 1950s, significant progress has been made toward an improved understanding of intrinsic charge transport phenomena in organic materials, and several models, such as the band model, the tight-binding model, and the hopping model, have been proposed for the simulation and prediction of low-density intrinsic transport behaviors in organic crystals.[14,15] Recently, based on the hopping model, Shuai et al. proposed a random walk approach to simulate the diffusion process of the charge carrier,[16] which has been widely applied in homogeneous and inhomogeneous thin film phases. In our simulations, we selected the random walk approach to calculate the diffusion coefficient in the studied organic semiconductors.

In this work, the electronic properties of **AQ** and its derivatives, as shown in Scheme 1, are systematically investigated. All the reorganization energies (λ) associated with charge transport are evaluated using the adiabatic potential-energy surface method, and the frequency dependence of mode-specific λ of **AQ**, $\mathbf{AQ}_{18}$, $\mathbf{AQ}_{23}$, and $\mathbf{AQ}_{27}$ is further calculated through the normal-mode (NM) analysis method. The influence of the site-specific substitution on the reorganization energy (λ), ionization potential (IP), and electronic affinity (EA) is discussed in detail. Furthermore, the electronic couplings of **AQ** and its derivatives are simulated, and the relationship between molecular packing structures and the electronic couplings are revealed through analyzing the effective coupling decided by the overlap between frontier molecular orbitals (FMOs). Based on the calculated λ values and intermolecular electronic couplings, the three-dimensional (3D) angular resolution anisotropic mobility for electron and hole transport is evaluated. Our calculations not only provide the quantitative predictions for the intrinsic carrier mobility in **AQ** derivatives but also offer a reference for the improvements of their OFET properties and further design of new n-type organic semiconductors.

2. COMPUTATIONAL METHODS

As one of the most important factors that govern the intermolecular charge transfer process in organic materials, the reorganization energy is mainly related to the geometric relaxation of the molecule (inner reorganization energy) and its surroundings (outer reorganization energy) on the movement of the charge carriers. In organic crystals, external reorganization energy is usually neglected because of the low dielectric constants of molecular solids and fortuitous cancellation of errors that includes neglect of tunneling contributions to the rate constants.[17,18] The inner reorganization energy λ associated with the charge transport process in organic semiconducting materials can be evaluated in two

https://doi.org/10.1021/acsomega.2c06591
ACS Omega 2022, 7, 48391−48402

ways.[19] The first is the adiabatic potential energy surface method, in which the λ can be expressed as follows:

$$\lambda = \lambda_1 + \lambda_2 = (E_{\pm}^{*} - E_{\pm}) + (E^{*} - E) \quad (1)$$

Here, E and $E_{\pm}$ represent the energies of the neutral and cation/anion species in their lowest energy geometries, respectively, and E^* and $E_{\pm}^*$ are the energies of the neutral and cation/anion species with the geometries of the cation/anion and neutral species, respectively. The other method is the normal-mode (NM) analysis method, which provides the partition of the total relaxation energy into the contributions from each vibrational mode:

$$\lambda = \Sigma \lambda_i = \Sigma(\omega_i \Delta Q_i^{2})/2 \quad (2)$$

where ΔQ_i represents the displacement along normal-mode Q_i between the equilibrium geometries of the neutral and charged molecules and ω_i is the corresponding frequency. The NM analysis and λ_i were obtained through the MOMAP program.[15,16,20−22]

From the adiabatic potential-energy surfaces of neutral/charged species, the vertical ionization potential (VIP), adiabatic ionization potential (AIP), vertical electronic affinity (VEA), and adiabatic electron affinity (AEA) can be calculated as follows:

$$\mathrm{VIP} = E^{+*} - E \quad (3)$$

$$\mathrm{AIP} = E^{+} - E \quad (4)$$

$$\mathrm{VEA} = E - E^{-*} \quad (5)$$

$$\mathrm{AEA} = E - E^{-} \quad (6)$$

Full geometry optimizations of the monomer molecules and the energy calculations are carried out using the B3LYP functional in conjunction with the 6-311G* basis set.[23]

The other key factor influencing the charger-transfer rate is intermolecular electronic couplings. In a symmetrically orthonormalized basis, the intermolecular electronic coupling V_{ij} takes the following form:

$$V_{ij} = |(J_{ij} - 0.5^{*}(e_i + e_j)^{*}S_{ij})/(1 - S_{ij}^{2})| \quad (7)$$

Here, the spatial overlap (S_{ij}), charge transfer integrals (J_{ij}), and site energies (e_i, e_j) can be written as

$$e_{i(j)} = \langle \Psi_{i(j)} | H | \Psi_{i(j)} \rangle \quad (8)$$

$$S_{ij} = \langle \Psi_i | \Psi_j \rangle \quad (9)$$

$$J_{ij} = \langle \Psi_i | H | \Psi_j \rangle \quad (10)$$

where H is the system Kohn−Sham Hamiltonian of the dimer system and $\Psi_{i(j)}$ means the highest occupied molecular orbitals (HOMOs) of the monomer (for hole transport) or lowest unoccupied molecular orbitals (LUMOs) of the monomer (for electron transport) with Löwdin's symmetric transformation that can be used as the orthogonal basis set for calculation.[24] All the calculations of all electronic couplings in different molecular dimers are implemented at the density functional theory (DFT) level using the B3LYP functional and 6-311G* basis set.

At room temperature, it is generally accepted that the charge carrier transport in organic materials takes place via charge hopping between adjacent molecules. The intermolecular hopping rate based on the Marcus−Hush theory in the high-temperature limit is as follows:[20]

$$W = \frac{V^2}{\hbar}\left(\frac{\pi}{\lambda k_B T}\right)^{1/2} \exp\left(-\frac{\lambda}{4k_B T}\right) \quad (11)$$

λ is the reorganization energy and V is the intermolecular effective electronic coupling. Assuming no correlation between charge hopping events and that charge motion is a homogenous random walk, the average drift mobility for charge carrier (hole/electron) transport in semiconductor materials can be simply written as •

$$\mu = e{\cdot}D/(k_B{\cdot}T) \quad (12)$$

where k_B is the Boltzmann· constant, T is temperature, and D is the diffusion coefficient of a charge carrier, which can be calculated through

$$D = (1/2n){\cdot}\mathrm{d}s/\mathrm{d}t \quad (13)$$

where n = 1, 2, or 3 is the dimensionality of the system under investigation; s is the mean-square displacement (MSD); and t is the simulation time. All the simulations of charge carrier mobility in 3D space are completed using the MOMAP transport package.

3. RESULTS AND DISCUSSION

3.1. Substitute-Site Effects on Electron Affinities (EAs) and Ionization Potentials (IPs). There are eight substitution positions in the **AQ** molecule: C_1, C_2, C_3, C_4, C_5, C_6, C_7, and C_8 site, as shown in Scheme 1. According to the molecular symmetry, C_1, C_4, C_5, and C_8 are equivalent, and they can be named as ortho-carbons. C_2, C_3, C_6, and C_7 are equivalent, and they can be named as meta-carbons. Thus, there existed 10 di-substituted **AQ** derivatives. Thereinto, the compounds **AQ14**, **AQ15**, and **AQ18** can be obtained by introducing two trifluoromethylethynyl groups at ortho-carbons; the compounds **AQ23**, **AQ26**, and **AQ27** can be obtained by introducing two trifluoromethylethynyl groups at meta-carbons; and the compounds **AQ12**, **AQ13**, **AQ16**, and **AQ17** can be obtained by introducing one trifluoromethyle-

Table 1. The Theoretical Adiabatic/Vertical Ionization Potentials (AIP/VIP), Adiabatic/Vertical Electron Affinities (AEA/VEA), and HOMO−LUMO Energy Gaps (E_{gap}) for the Compound AQ and Its Derivatives

molecular crystals	AIP (eV)	VIP (eV)	AEA (eV)	VEA (eV)	E_{gap} (eV)
AQ	8.96	9.01	1.55	1.37	4.24
AQ14	8.78	8.97	2.32	2.11	3.88
AQ15	8.86	8.96	2.32	2.12	3.80
AQ18	8.86	8.98	2.34	2.14	3.90
AQ12	8.91	9.06	2.35	2.16	3.95
AQ13	8.94	9.11	2.44	2.25	3.94
AQ16	8.93	9.03	2.41	2.22	3.94
AQ17	8.93	9.04	2.42	2.23	3.95
AQ23	8.99	9.11	2.50	2.32	3.95
AQ26	8.94	9.05	2.50	2.32	3.94
AQ27	8.94	9.04	2.49	2.31	3.93
AQ1458	8.80	8.92	2.91	2.64	3.66
AQ2367	9.02	9.13	3.16	2.99	3.64

https://doi.org/10.1021/acsomega.2c06591
ACS Omega 2022, 7, 48391−48402

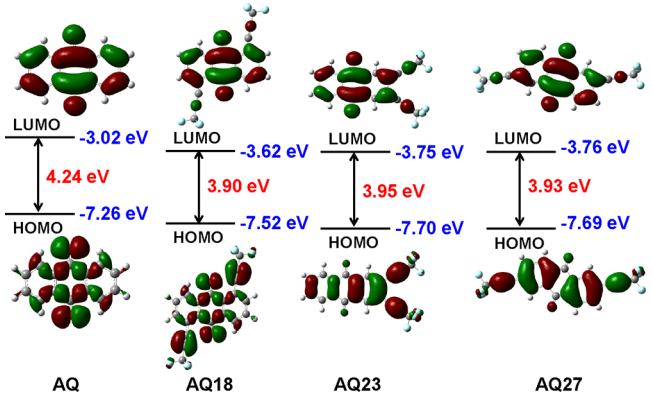

Figure 1. The HOMO and LUMO distributions, energies, and HOMO−LUMO energy gaps for **AQ**, **AQ18**, **AQ23**, and **AQ27**.

Table 2. Reorganization Energies (eV) Associated with Intermolecular Hole-Transfer (λ_h) and Electron-Transfer (λ_e) for AQ and Its Derivatives Are Evaluated by the Adiabatic Potential Energy Surface (APES) Method and Normal-Mode Analysis (NMA) Method

	λ_h (eV)		λ_e (eV)	
molecular crystals	APES	NMA	APES	NMA
AQ	0.122	0.137	0.350	0.350
AQ14	0.369		0.414	
AQ15	0.212		0.399	
AQ18	0.238	0.254	0.401	0.402
AQ12	0.294		0.380	
AQ13	0.572		0.384	
AQ16	0.199		0.379	
AQ17	0.225		0.381	
AQ23	0.249	0.250	0.355	0.356
AQ26	0.213		0.358	
AQ27	0.204	0.205	0.357	0.357
AQ1458	0.224		0.485	
AQ2367	0.210		0.331	

thynyl group at ortho-carbons and the other trifluoromethylethynyl group at meta-carbons.

In general, EAs are related to the energy of the LUMO in a one-electron picture. The organic semiconducting materials with high EAs usually have relatively low-energy lowest unoccupied molecular orbitals (LUMOs) and can be more readily reduced than the ones with low EAs. Therefore, they can be used widely in applications where charge needs to be electrically injected rather than photogenerated.[10] For the design of new-type electronic materials, EAs are generally regarded as essential prerequisites because they are related to the injection efficiency of electrons into the LUMOs and the material stability under processing/ambient operating conditions.

The EAs for the compound **AQ** and its derivatives are summarized in Table 1. It can be seen that the EA values of di-substituted **AQ** derivatives are about 0.7−1.0 eV higher than those of the **AQ** (1.55 eV), which indicates that the introduction of the trifluoromethylethynyl group could largely decrease the LUMO energy of **AQ** as a result of the negative conjugation effect. Interestingly, the **AQ** derivatives with trifluoromethylethynyl groups attached to meta-carbons show larger EA values than the ones with trifluoromethylethynyl groups attached to ortho-carbons. As shown in Table 1, the

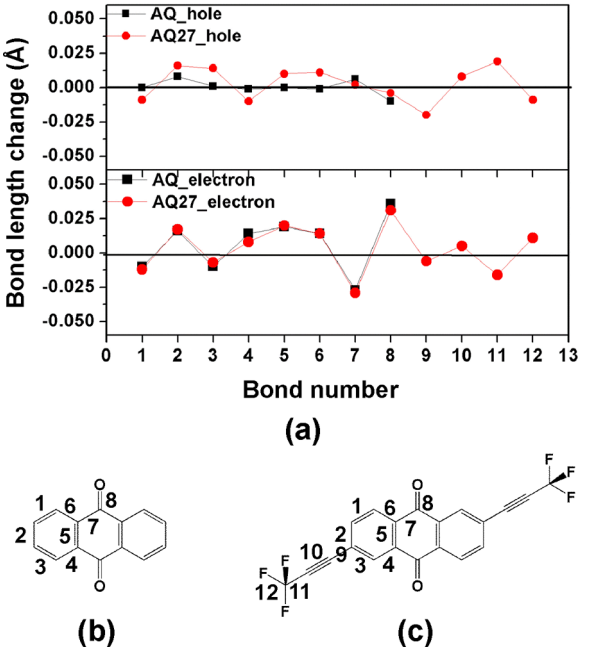

Figure 2. (a) Calculated C−C bond (1−8) length changes in **AQ** and C−C bond (1−12) and C−F bond (13) length changes in **AQ27** during the hole- and electron-transfer process and the labels of different C−C bonds in (b) **AQ** and (c) **AQ27**.

AEA values of **AQ23**, **AQ26**, and **AQ27** are 2.50, 2.50, and 2.49 eV, respectively, which are about 0.15−0.18 eV higher than those of **AQ14** (2.32 eV), **AQ15** (2.35 eV), and **AQ18** (2.34 eV). As we know, the injection efficiency of electrons into the LUMO and the material stability under processing/ambient operating conditions could be improved by increasing EA values; therefore, the meta-substitution of trifluoromethylethynyl groups in **AQ** is more beneficial to the improvement in the ambient stability of **AQ**.

To clarify the electronic effect induced by a different substitute site, the distributions of lowest unoccupied molecular orbitals (LUMOs) of **AQ18** and **AQ23** are further analyzed. As shown in Figure 1, both molecules show similar distribution characters: the LUMOs mainly localized on the **AQ** core, and the carbon atoms linked with trifluoromethyl. However, there is a slight difference at the link between the **AQ** core and substitute groups. The LUMOs localized on the **AQ** core were extended to the adjacent carbon atom in substituents for the **AQ23**. The extension of the LUMO delocalization range in **AQ23** suggests that the $\pi-\pi$ conjugative effect induced by trifluoromethylethynyl would further strengthen from **AQ18** to **AQ23**. The larger negative conjugation effect could effectively lower the LUMO energy, which reasonably explains substitute-site effects on EA values.

From the optimized structures of **AQ18** and **AQ23**, we can also find that the bond angles C_1-C_{15}-C_{16} and C_{15}-C_{16}-C_{17} in **AQ18** are 172° and 176°, respectively; by contrast, the bond angles C_2-C_{15}-C_{16} and C_{15}-C_{16}-C_{17} in **AQ23** are 179° and 180°, respectively (C atom labeling can be seen in Scheme 1). It indicates that the trifluoromethylethynyl group in **AQ23** still maintained a linear shape, whereas the linear molecular structure of the trifluoromethylethynyl group in **AQ18** is slightly bent, which weakens the conjugative effect between the **AQ** core and substitute group. In addition, the C_2-C_{15} bond length in **AQ23** (1.422 Å) is slightly shorter than the C_1-C_{15}

https://doi.org/10.1021/acsomega.2c06591
ACS Omega 2022, 7, 48391−48402

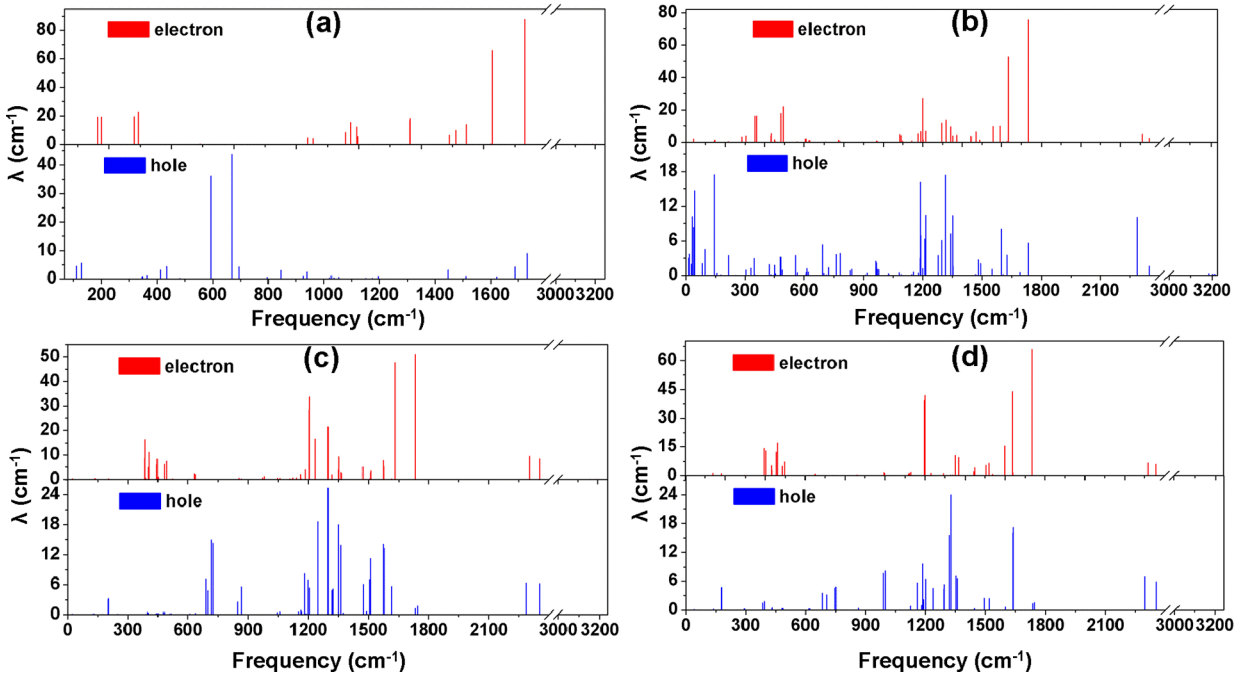

Figure 3. Frequency dependence of reorganization energies of (a) **AQ**, (b) **AQ18**, (c) **AQ23**, and (d) **AQ27** upon the electron-transfer process and hole-transfer process.

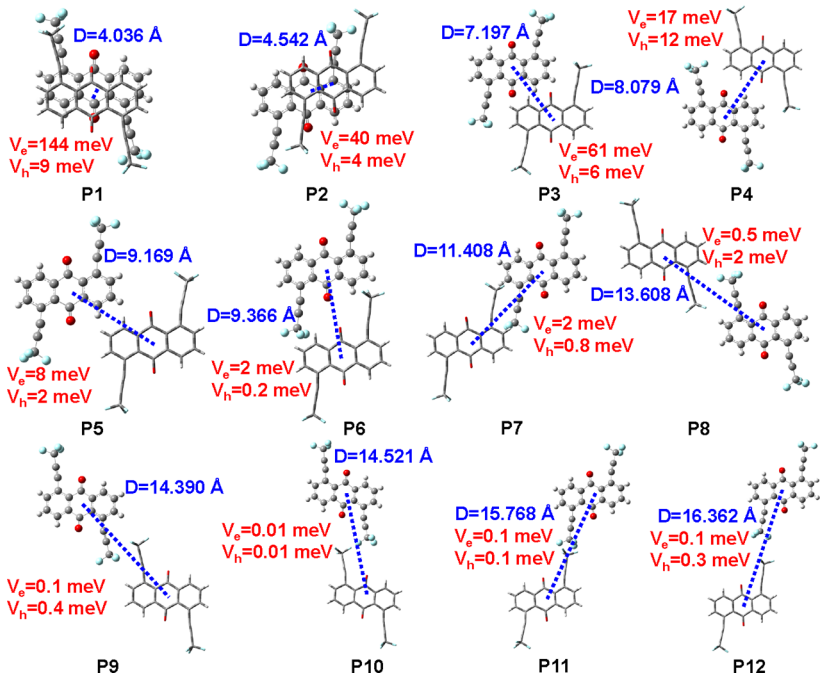

Figure 4. Relative position of two monomers, the intermolecular mass-centered distance D, and the electronic couplings for the electron transfer (V_e) and hole transfer (V_h) in P_1–P_{12} dimers of **AQ18**.

bond length in **AQ18** (1.426 Å), which provides another evidence for the stronger conjugation effect in **AQ23**. The dependence of substituent structures on the substitute site is mainly related to the steric hindrance. In **AQ18**, the distance between O and the nearest-neighbor C_{15} is about 2.696 Å, which is much shorter than the sum of the van der Waals radius of C and O (3.12 Å). The repulsive interactions between C_{15} and O lead to the bent geometry of trifluoromethylethynyl groups. In **AQ23**, the large distance between O and the nearest-neighbor C_{15} (5.07 Å) has almost no effect on trifluoromethylethynyl groups.

We further calculate the tetra-substituted derivatives of **AQ**. As shown in Table 1, the AEA value of **AQ2367** is 3.16 eV, which is about 0.66 eV larger than the ones of **AQ23**, **AQ26**, and **AQ27**, and the AEA value of **AQ1458** is 2.91 eV, which is about 0.57 eV larger than the ones of **AQ14**, **AQ15**, and **AQ18**. The calculations show that the electron-injection barrier of **AQ** decreases markedly with the increase in the

https://doi.org/10.1021/acsomega.2c06591
ACS Omega 2022, 7, 48391−48402

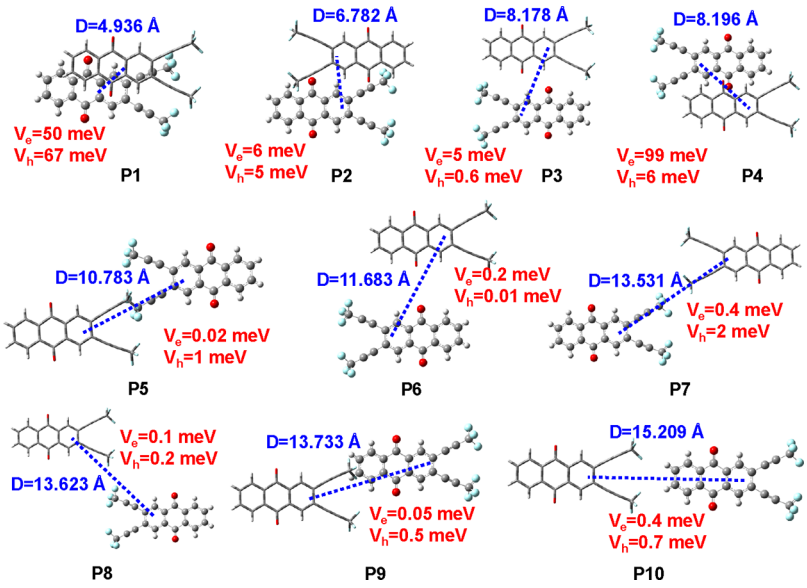

Figure 5. Relative position of two monomers, the intermolecular mass-centered distance D, and the electronic couplings for the electron transfer (V_e) and hole transfer (V_h) in P_1−P_{10} dimers of **AQ23**.

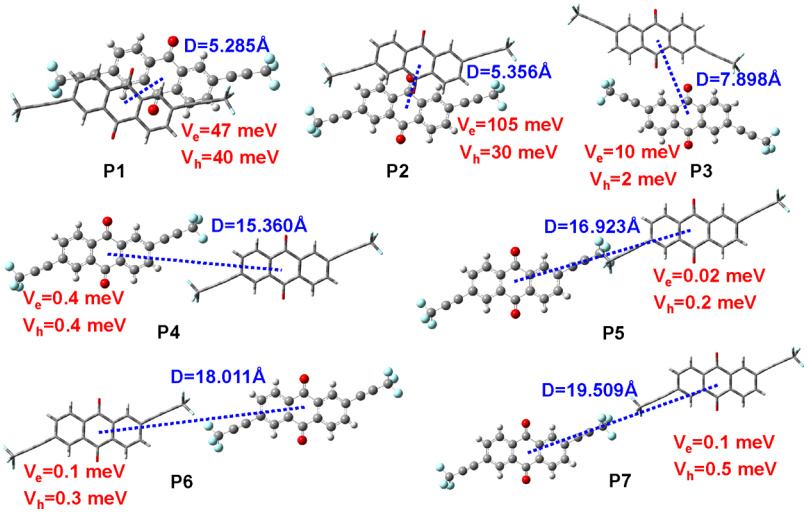

Figure 6. Relative position of two monomers, the intermolecular mass-centered distance D, and the electronic couplings for the electron transfer (V_e) and hole transfer (V_h) in P_1−P_7 dimers of **AQ27**.

Table 3. Simulated Hole ($\bar{\mu}$) and Electron (μ^+) Mobilities ($cm^2 \cdot V^{-1} \cdot s^{-1}$) for AQ18, AQ23, AQ27, and Some Experimental Data

molecular crystals.	μ^+	$\bar{\mu}$	experimental μ^-
AQ18	0.005−0.11	0.0004−0.31	$(4.5 \pm 2.0) \times 10^{-4}$[a] (highest: 0.0021)
AQ23	0.001−0.96	9×10^{-4}−0.32	0.029 ± 0.010[a] (highest: 0.042)
AQ27	0.19−4.45	0.035−0.82	0.087 ± 0.072[a] (highest: 0.28)

[a]Reference 12.

number of trifluoromethylethynyl groups, and the optimal substitute sites are the meta-carbons of **AQ**.

The IP values of **AQ** and its derivatives are also summarized in Table 1. The adiabatic IP values of the di-substituted **AQ** derivatives lie between 8.78 and 8.99 eV, which are very close to the one of **AQ** (8.96 eV). It indicates that the introduction of the trifluoromethylethynyl group has a slight influence on the IP values. It also means that the addition of the trifluoromethylethynyl group has a small influence on the energy barrier of hole injection.

Moreover, the energies of HOMO (E_{HOMO}) and LUMO (E_{LUMO}) of **AQ**, **AQ18**, **AQ23**, and **AQ27** are presented in Figure 1. Our calculation results are consistent with the DFT calculated values at the 6-311++G(d,p) level by Zhao et al.[12] The E_{HOMO} decreases as follows: **AQ** (−7.26 eV) > **AQ18** (−7.52 eV) > **AQ23** (−7.70 eV) and **AQ27** (−7.69 eV), and the E_{LUMO} decreases as follows: **AQ** (−3.02 eV) > **AQ18** (−3.62 eV) > **AQ23** (−3.75 eV) and **AQ27** (−3.76 eV), which indicate that the substitution of trifluoromethylethynyl leads to the lower HOMO and LUMO energy levels, and the meta substitution is more beneficial to the decrease of FMO energy. Our calculation results are consistent with the DFT calculated values at the 6-311++G(d,p) level by Zhao et al.[12] The HOMO−LUMO energy gaps (E_{gap}) of **AQ** and its derivatives are shown in Table 1. The E_{gap} values decrease in

https://doi.org/10.1021/acsomega.2c06591
ACS Omega 2022, 7, 48391−48402

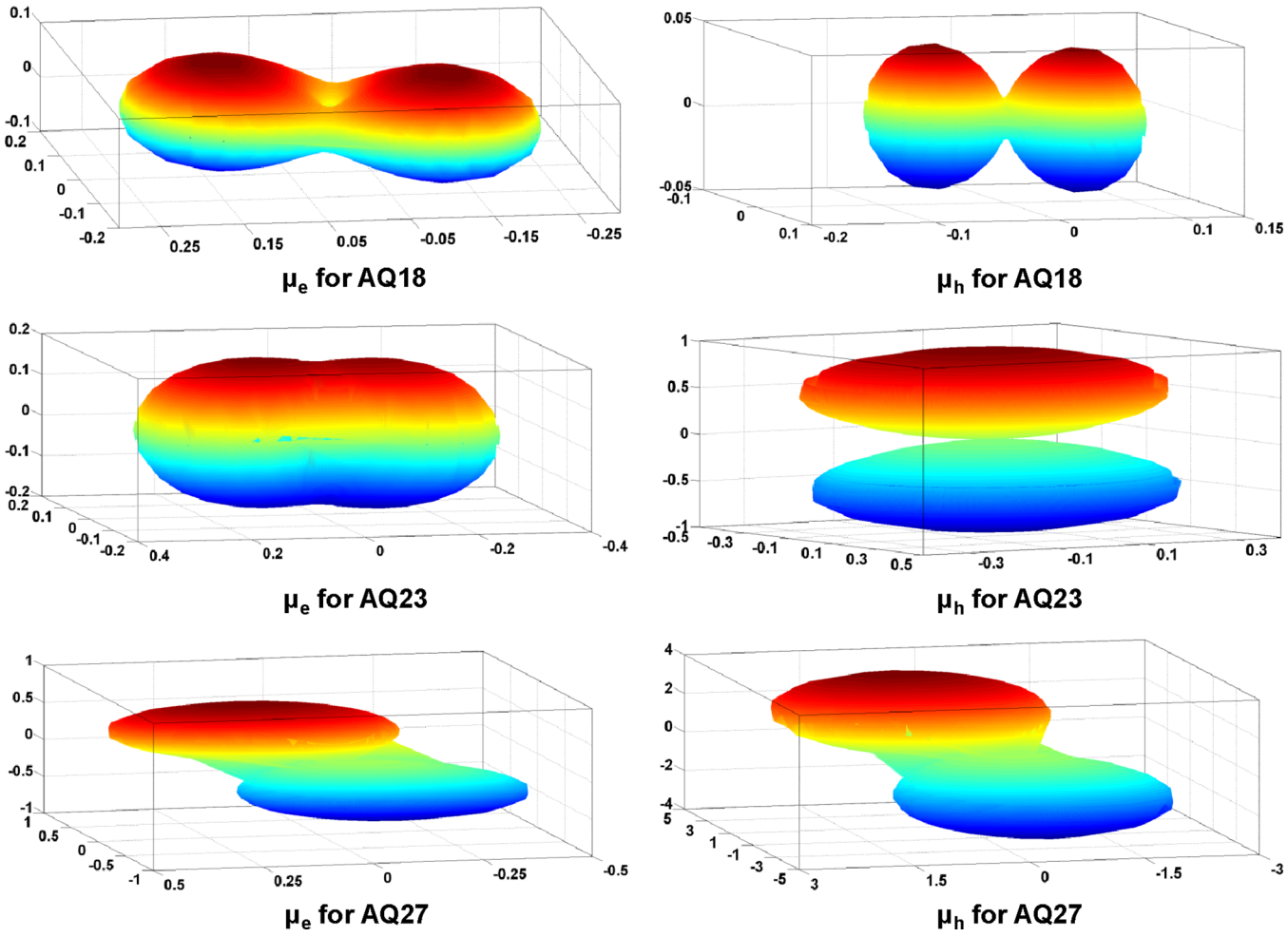

Figure 7. Calculated angle-resolved anisotropic electron-mobility values μ_e ($cm^2 \cdot V^{-1} \cdot S^{-1}$) for **AQ18**, **AQ23**, and **AQ27** in three-dimensional space and angle-resolved anisotropic hole-mobility values μ_h ($cm^2 \cdot V^{-1} \cdot S^{-1}$) for **AQ18**, **AQ23**, and **AQ27** in three-dimensional space.

the following order: **AQ** (4.24 eV) > di-substituted **AQ** derivatives (3.80−3.95 eV) > tetra-substituted **AQ** derivatives (3.64−3.66 eV), which suggest that the substitution of trifluoromethylethynyl groups leads to the narrower E_{gap}, and the decrease of E_{gap} shows a positive correlation with the number of substitute groups.

3.2. Substitute-Site Effects on Reorganization Energies. The influence of the substitute group on the λ of **AQ** is pronouncedly dependent on two factors: the change in molecular rigidity and the increase of additional vibrational degrees of freedom, both of which might make a significant contribution to the total λ values. During the intermolecular hole/electron-transfer process, if the introduction of the substitute groups effectively enhances the plane rigidity of the **AQ** core, the geometry relaxations of the **AQ** core upon oxidation/reduction process would be weakened; as a result, the corresponding λ of the **AQ** core can be decreased. Conversely, the introduction of substitute groups leads to the large geometry relaxations of the **AQ** core, which increase the λ value of the **AQ** core. On the other hand, the addition of substitute groups could increase the vibrational degrees of freedom, and the geometry relaxations of the substitute groups would induce the larger λ values of **AQ** derivatives than the one of **AQ**.

Table 2 shows the λ values for **AQ** and its derivatives. The calculation results show that the λ values associated with the hole-transport process (λ_h) of trifluoromethylated **AQ** are about 1.6−4.7 times larger than those of **AQ**, suggesting that trifluoromethylation of **AQ** greatly increases the resistance of hole transport, and it is unfavorable for its field-effect transistor properties as a p-type material. To clarify the major factor responsible for the increase in λ_h values, the compounds **AQ** and **AQ27** are taken as examples to analyze the effect of the substituent group on the λ_h of **AQ**. Figure 2 shows the geometric variations of an isolated **AQ** and **AQ27** in the hole-transfer process. It is easy to see that the C−C/C═C bonds in bilateral phenyl rings of **AQ** undergo geometric changes to a small extent, and most of them have almost no changes (<0.008 Å), which means that the stretching vibrations of C−C/C═C bonds in phenyl rings contribute little to λ_h value. In comparison, most C−C/C═C bonds in bilateral phenyl rings of **AQ27** undergo geometric changes in a range of 0.01 Å−0.016 Å, which is much larger than that in **AQ**. Thus, the vibration modes related to C−C/C═C bond relaxations should contribute much to the total λ_h of **AQ27**.

The frequency dependence of mode-specific reorganization energies for compounds **AQ** and **AQ27** are shown in Figure 3a,d. We can see that the contributions to the λ_h of compound **AQ** mainly come from low-frequency modes below 1000 cm^{-1} (83% of the total relaxation energy originates from vibrational modes at about 1000 cm^{-1} or lower) and that the contributions to the λ_h of compound **AQ27** mainly come

https://doi.org/10.1021/acsomega.2c06591
ACS Omega 2022, 7, 48391−48402

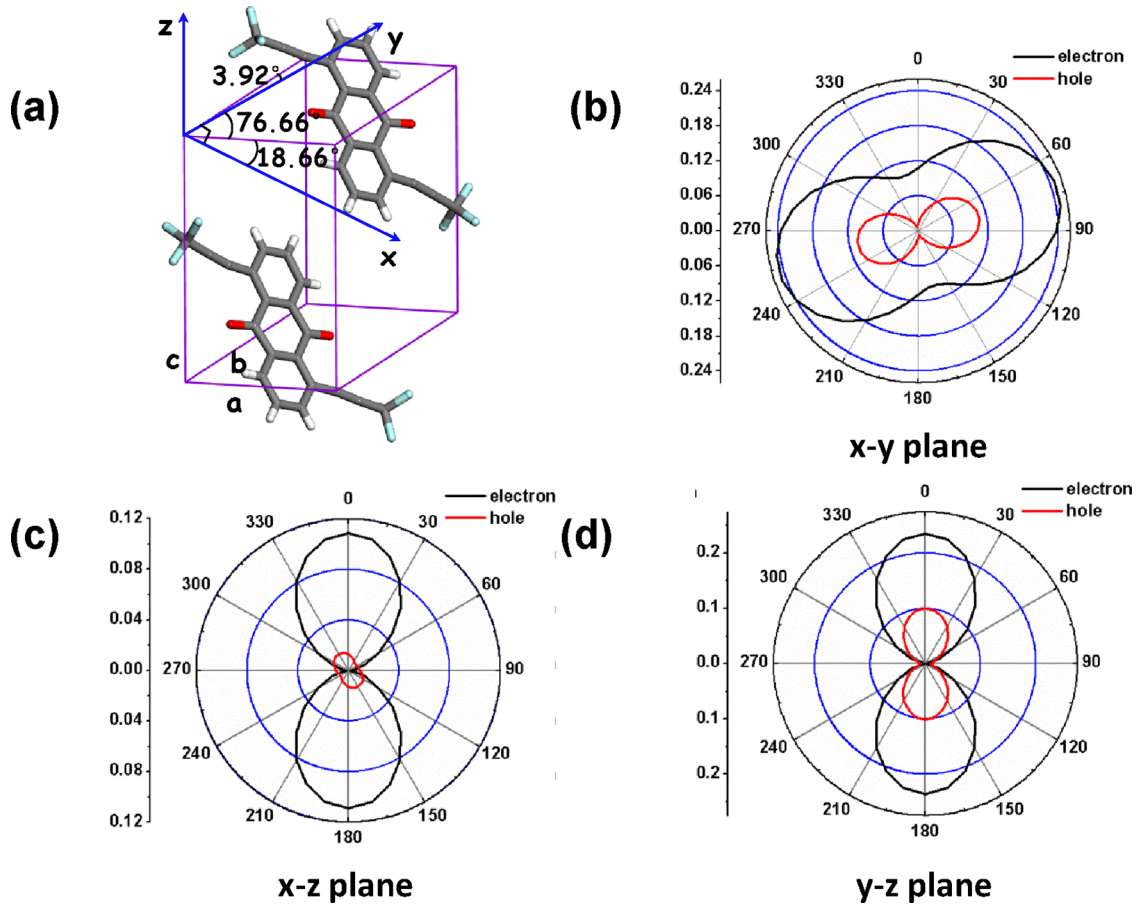

Figure 8. (a) Crystal structure of **AQ18** and the Cartesian coordinate system corresponding to the mobility simulation and the calculated angle-resolved anisotropic hole mobility (red line) and electron mobility (black line) of **AQ18** in the (b) *xy* plane, (c) *xz* plane, and (d) *yz* plane.

from high-frequency modes above 1000 cm^{-1} (76% of the total relaxation energy originates from vibrational modes at about 1000 cm^{-1} or higher). The detailed analysis shows that most of these high-frequency modes are associated with the stretching vibration of chemical bonds and that most of these low-frequency modes are related to the bending vibrations of chemical bonds. The largest contributions to the λ_h of compound **AQ** mainly come from the vibration modes at 670.6 (43.8) and 592.6 cm^{-1} (36.2 meV), which correspond to the out-of-plane wagging vibrations. For compound **AQ27**, the total λ_h mainly comes from three parts: (i) the scissoring vibration modes of the **AQ** core, such as the vibration modes at 988.38 (7.7), 998.5 (8.2), and 1185.4 cm^{-1} (9.6 meV); (ii) the symmetric stretching vibrations of C−C/C═C bonds in the **AQ** core, such as the vibration modes at 1318.65 (15.6), 1328.17 (24.1), 1352.79 (7.1), 1637.66 (16.1), 1637.66 (16.1),and 1639.47 cm^{-1} (17.1 meV); and (iii) symmetric stretching vibrations of C−C/C≡C bonds in substitute groups, such as the vibration modes at 1328.17 (24.1) and 2298.07 cm^{-1} (7.0 meV). Through analyzing the contributions of different vibration modes to the reorganization energies of **AQ** and **AQ27**, we can conclude that the introduction of trifluoromethylethynyl groups not only increases λ_h of the **AQ** core by about 33 meV but also makes an additional contribution to the total λ_h by about 49 meV due to the symmetric stretching vibrations of C−C/C≡C bonds in trifluoromethylethynyl groups.

Different from the λ_h, the reorganization energies related to the electron-transport process (λ_e) for **AQ** and its derivatives show an obvious regularity: (i) almost similar λ_e values in **AQ** and meta-substituted **AQ** derivatives can be observed, and (ii) the λ_e values of ortho-substituted derivatives are about ∼50 meV larger than the ones of meta-substituted derivatives. As shown in Table 2, the λ_e values of **AQ23**, **AQ26**, and **AQ27** are 355, 358, and 357 meV, respectively, which are very similar with the one of **AQ** (350 meV), whereas the λ_e values of **AQ14**, **AQ15**, and **AQ18** are 414, 399, and 401 meV, respectively. These indicate that the λ_e values are strongly affected by substitution sites. We take **AQ**, **AQ18**, and **AQ27** as examples to analyze the influence of substitute sites on the λ_e value. The frequency dependence of mode-specific reorganization energies for **AQ**, **AQ18**, and **AQ27** is depicted in Figure 3a,b,d. We can see that the contributions to the λ_e of compounds **AQ**, **AQ18**, and **AQ27** mainly come from high-frequency modes above 1000 cm^{-1}: 77, 73, and 75% of the total relaxation energy of compounds **AQ**, **AQ18**, and **AQ27**, respectively, originate from vibrational modes at about 1000 cm^{-1} or higher. The largest contributions to the λ_e of compound **AQ** mainly come from the vibration modes at 1626.44 (65.9) and 1730.17 cm^{-1} (87.6 meV), which correspond to the stretching vibration of C═O bonds along the short molecular axis. Similarly, the 1638.48 cm^{-1} mode in the anion state (43.8 meV) and the 1734.71 cm^{-1} mode in the neutral state (66.0 meV), which have largest contributions to the total λ_e of compound **AQ27**, correspond to the stretching

https://doi.org/10.1021/acsomega.2c06591
ACS Omega 2022, 7, 48391−48402

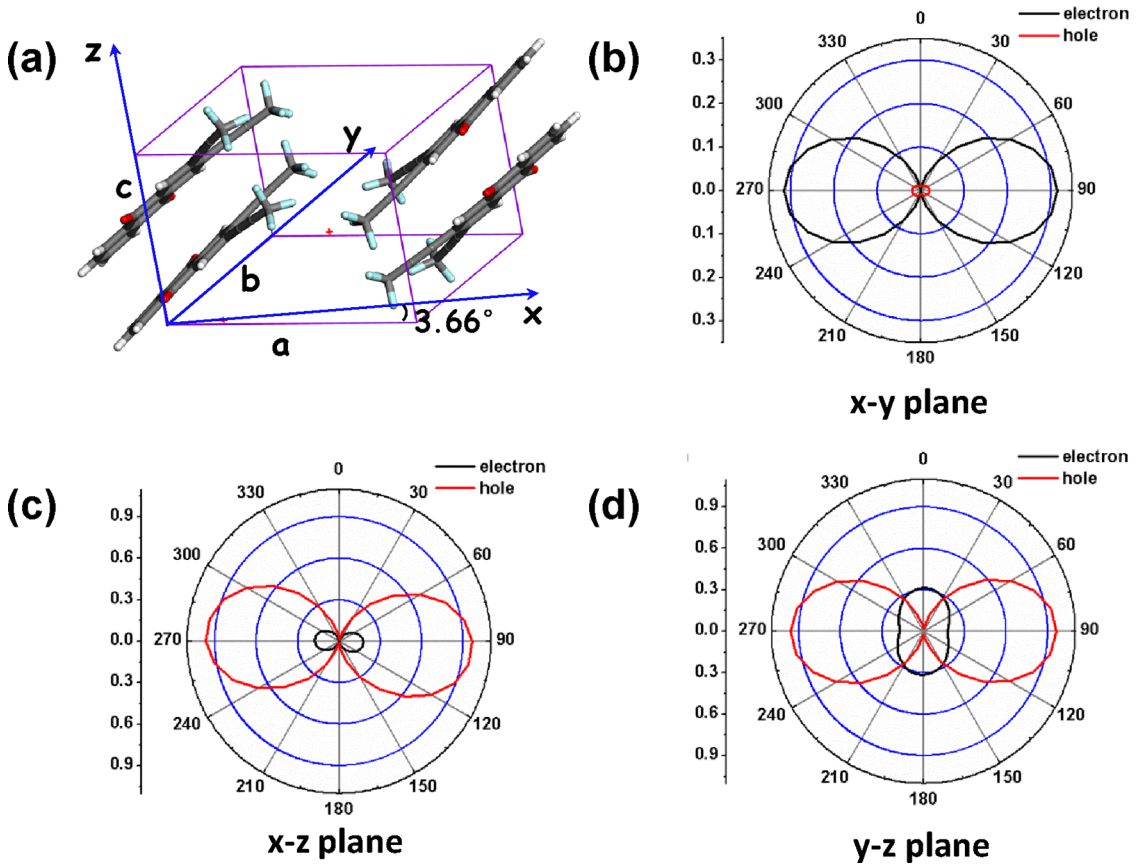

Figure 9. (a) Crystal structure of **AQ23** and the Cartesian coordinate system corresponding to the mobility simulation and the calculated angle-resolved anisotropic hole mobility (red line) and electron mobility (black line) of **AQ23** in the (b) *xy* plane, (c) *xz* plane, and (d) *yz* plane.

vibration of C═O bonds along the short molecular axis, and the 1632.65 cm^{-1} mode in the anion state (52.7 meV) and the 1734.59 cm^{-1} mode in the neutral state (75.6 meV), which have largest contributions to the total λ_e of compound **AQ18**, correspond to the stretching vibration of C═O bonds along the short molecular axis. It is easy to conclude that the contributions of stretching vibration in C═O to total λ_e values are partly lessened by the addition of trifluoromethylethynyl groups, especially for meta-substituted derivative **AQ27**. Besides, the contributions of the C−C/C═C bond stretching vibrations in **AQ** to the λ_e value also decrease with the introduction of trifluoromethylethynyl groups. For example, the vibration modes at 1362.91 and 1363.28 cm^{-1}, which correspond to C−C/C═C bonds' stretching vibrations of bilateral phenyl rings, contribute about 16.7 and 18.3 meV, respectively, to the λ_e value of **AQ**; in comparison, the C−C/C═C bonds' stretching vibrations in bilateral phenyl rings with vibration modes at 1352.79 and 1370.41 cm^{-1} contribute about 10.7 and 9.6 meV, respectively, to the λ_e value of **AQ27**. As shown in Figure 2, the geometric variations of an isolated **AQ** and **AQ27** in the electron-transfer process also show that the relaxation range of C−C/C═C bonds and the C═O bonds in the **AQ** core of **AQ27** is slightly smaller than the one in **AQ**. The weaker geometry relaxations of the **AQ** core suggest that the introduction of trifluoromethylethynyl groups pushes the λ_e value of the **AQ** core to be smaller than that of the molecule **AQ**.

On the other hand, the C−C/C≡C bonds' bending vibrations and stretching vibrations of trifluoromethylethynyl groups contribute much to the λ_e value of trifluoromethylated **AQ**. For example, the C−C bonds' bending vibrations with vibration modes at 454.27 and 460.88 cm^{-1} contribute about 12.1 and 17.0 meV, respectively, to the λ_e value of **AQ27**, and the C−C bonds' stretching vibrations with vibration modes at 1197.89 and 1201.44 cm^{-1} contribute about 14.0 and 29.9 meV, respectively, to the λ_e value of **AQ27**.

For further elucidating substitute-site effects on the λ_e values, we comparatively analyze the influence of ortho- and meta-substitutions on the **AQ** core of **AQ18** and **AQ27**. As shown in Figure 4b,d, decomposition of the λ_e of **AQ18** and **AQ27** into individual contributions from the relevant vibrational modes indicates that the vibration modes' corresponding torsion vibration and stretching vibrations of the center benzoquinone ring make more contributions to the λ_e of **AQ18** than the λ_e value of **AQ27**. For example, the vibration modes at 486.07 and 497.21 cm^{-1}, which correspond to C═O bonds' torsion vibrations in benzoquinone rings, contribute about 17.8 and 22.1 meV, respectively, to the λ_e value of **AQ18**. In comparison, the C═O bonds' torsion vibrations with vibration modes at 486.07 and 497.21 cm^{-1} contribute about 5.1 and 7.3 meV, respectively, to the λ_e value of **AQ27**; the C−C bonds' stretching vibrations with vibration modes at 1294.66 and 1316.65 cm^{-1} contribute about 11.7 and 13.5 meV, respectively, to the λ_e value of **AQ18**; and the C−C bonds' stretching vibrations with vibration modes at 1292.91 and 1308.62 cm^{-1} contribute only 1.1 and 0.1 meV, respectively, to the λ_e value of **AQ27**. As in the previous analysis, the C═O stretching vibrations in the **AQ** core also contribute more to the λ_e value of **AQ18** (128.3 meV) than to the λ_e value of **AQ27** (109.8 meV). For **AQ27**, the increase in λ_e of the

https://doi.org/10.1021/acsomega.2c06591
ACS Omega 2022, 7, 48391−48402

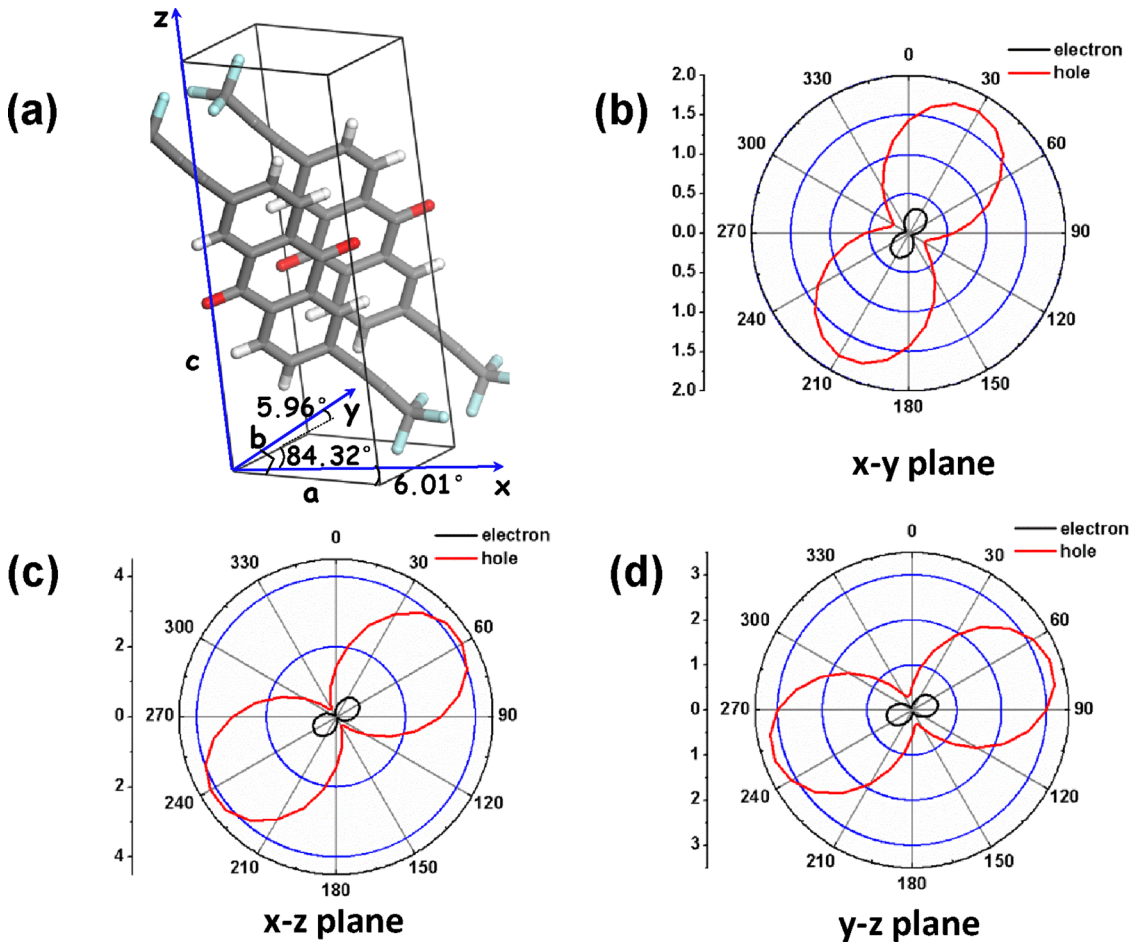

Figure 10. (a) Crystal structure of **AQ27** and the Cartesian coordinate system corresponding to the mobility simulation and the calculated angle resolved anisotropic hole mobility (red line) and electron mobility (black line) of **AQ27** in the (b) *xy* plane, (c) *xz* plane, and (d) *yz* plane.

substituted trifluoromethylethynyl groups can be mostly canceled by the decrease in λ_e of the **AQ** core; as a result, the total λ_e value of **AQ27** is similar with the one of **AQ**. In comparison, the decrease in λ_e of the **AQ** core induced by ortho-substitution (**AQ18**) is smaller than the one induced by meta-substitution (**AQ27**), and thus, the λ_e values of ortho-substituted **AQ** derivatives are about 50 meV larger than the ones of meta-substituted derivatives. We also evaluate the λ_e values of **AQ1458** and **AQ2367**, as shown in Table 2. We can see that the λ_e value of **AQ2367** is 0.331 eV, which is 0.154 eV smaller than the one of **AQ1458**, suggesting that the substitute sites have more effect on λ_e values with the increase in the number of trifluoromethylethynyl groups.

3.3. Electronic Couplings and Charge Carrier Mobilities. In the crystal structures of **AQ18**, **AQ23**, and **AQ27** prepared by Zhao et al., **AQ23** and **AQ27** are packed in a brickwork arrangement, and the **AQ18** exhibits one-dimensional $\pi-\pi$ stacking. The charge hopping pathways from the center molecule to its neighbors can be regarded as charge hopping between adjacent molecules of the dimers, and thus, the various types of charge hopping routes are simplified as different dimers. To facilitate the discussion below, the face-to-face intermolecular packing modes in crystals are defined as a P_n (n = 1, 2, ...) dimers, as shown in Figures 4–6. For **AQ18**, **AQ23**, and **AQ27**, the calculated electronic couplings for the electron transfer (V_e) and hole transfer (V_h) and the mass-centered distance D in the P_n dimers are depicted in Figures 4–6. As shown in Figure 4, the maximum V_e value appears in the P_1 dimer of **AQ18** (144 meV); in comparison, the V_h value in the P_1 dimer is only 9 meV. In the P_1 dimer, about 0.5 benzene ring displacement occurred between the neighboring **AQ18** monomers along the short molecular axis direction as a result of the steric hindrance effect between substitute groups. This displacement could effectively reduce the repulsion force between adjacent CF_3 groups and change the overlap between FMOs. The HOMOs distribute in the **AQ18** molecular plane and show an obvious σ bonding orbital character (see Figure 1), which is similar with the HOMO distributions of **AQ**; in comparison, the LUMO distributions are perpendicular to the **AQ18** molecular plane and show a π^* antibonding orbital character. For the HOMOs, the perfectly cofacial configuration and much short distance of the dimer are critical for the large intermolecular orbital overlap between neighboring molecules, and a relative displacement along the short or long molecular axis direction will result in the compensation of bonding and antibonding interactions or the decrease in overlap between HOMOs. For the LUMOs, the perfectly cofacial configuration of the dimer will lead to the large cancellation effect between the bonding and antibonding overlaps, which results in a weak intermolecular orbital overlap between neighboring molecules, and a suitable relative displacement along the short or long molecular axis direction, such as the 0.5–1 benzene ring, is favorable to the effective overlap between the LUMOs. These different distribution characteristics of the HOMOs and

https://doi.org/10.1021/acsomega.2c06591
ACS Omega 2022, 7, 48391–48402

LUMOs and the relative displacement in the P_1 dimer well explain the strong electronic coupling for electron transfer and weak electronic coupling for hole transfer in the P_1 dimer (see Figure S1). The maximum electronic couplings for hole transfer appeared in the P_4 dimer (12 meV), and the corresponding electronic coupling for electron transfer in the P_4 dimer is about 17 meV. These weak electronic couplings are related to the small overlap between the electronic wavefunctions of adjacent **AQ18** molecules due to the large intermolecular distance (8.079 Å).

As shown in Figure 5, the maximum V_e value appears in the P_4 dimer of **AQ23** (99 meV); in comparison, the V_h value in the P_4 dimer is only 6 meV. The maximum V_h appears in the P_1 dimer (67 meV), and the V_e in the P_1 dimer is about 50 meV. As shown in Figure 1, the HOMO and LUMO distributions are perpendicular to the **AQ23** molecular plane, which show an obvious π bonding orbital character and π^* antibonding orbital character, respectively. The HOMO distribution character of **AQ23**, quite different from **AQ18**, is spatially favorable for the enhancement of intermolecular electronic couplings. The HOMO of **AQ23** was mainly located on benzene ring C═C bonds and partially on the C≡C bonds, which were aligned predominantly along the short molecular axis, whereas the LUMOs were mainly located on the formally intraring C−C single bonds and on the O atoms, which were aligned predominantly along the long axis. These distribution characteristics of the HOMOs and LUMOs lead to the appearance of oscillations in the values of the electronic couplings, as one molecule in the perfectly cofacial dimer was translated along its long or short molecular axis. In dimer P_4, there was a displacement of more than one benzene ring along the short molecular axis. In this configuration, the V_h was dramatically reduced because of the reduction in the overall extent of spatial overlap between the two monomers caused by the relatively large displacement between two monomers (8.196 Å); by contrast, the decrease in the V_e was relatively small owing to the large overlap between the LUMOs localized on the O atoms and C═C bonds (see Figure S2). In the P_1 dimer, the small distance between two monomers (4.936 Å) increases the overall extent of spatial overlap between the two monomers; moreover, the suitable relative displacement along the molecular axis effectively avoids an excessive bonding−antibonding overlap pattern of the HOMO or LUMO wavefunctions in the dimers; as a result, the P_1 dimer shows strong electronic couplings for hole transfer (67 meV) and electron transfer (50 meV).

As shown in Figure 6, the V_h and V_e in P_1 and P_2 dimers of **AQ27** are much larger than those in other P-type dimers, which are related to the small intermolecular distance in P_1 and P_2 dimers. The intermolecular distances in P_1 and P_2 dimers are about 5.285 and 5.356 Å, respectively, which are much shorter than the ones in other dimers (7.898−19.509 Å). Similar with **AQ23**, the HOMO was mainly located on ring C−C/C═C bonds and the C≡C bonds aligned predominantly along the short molecular axis, whereas the LUMOs were mainly located on the formally intraring C−C/C═C bonds and the O atoms aligned predominantly along the long axis (see Figure 1). Although an obvious displacement between two neighboring molecules of the P_1 and P_2 dimers along the molecular axis direction leads to a decrease in the effective coupling projected area, the overlap between the FMOs localized on the edges of molecules contributes much to the V_h and V_e (see Figure S3). The maximum V_e value appeared in the P_2 dimer (105 meV), and maximum V_h value appeared in the P_1 dimer (40 meV).

The drift mobility of the holes/electrons in the single crystals of **AQ18**, **AQ23**, and **AQ27** was estimated from eq 12 by using the reorganization energies and effective electronic coupling matrix elements based on quantum mechanical (QM) calculations. The estimated ranges of the mobility in 3D space are summarized in Table 3. The simulated data for the electron-transfer mobility agree well with the experimental results under room temperature, suggesting that our computation method and strategy used here are reasonable. The anisotropic hole-transfer and electron-transfer mobility values in three-dimensional space are shown in Figure 7. It can be found that the hole and electron mobility in single crystals of **AQ18**, **AQ23**, and **AQ27** shows a remarkable anisotropic behavior. For **AQ18** and **AQ27**, the hole-transfer mobility and electron-transfer mobility show a similar anisotropic behavior, which means that the highest hole and electron mobilities can be achieved in the same transistor channel of OFET, whereas the hole mobility and electron mobility in the single crystal of **AQ23** show quite different anisotropic behavior, and the optimal hole and electron mobilities appear in different conductive channels. These distribution characters are related to the relative magnitudes of intermolecular electronic couplings. For example, the major V_h and V_e values in the **AQ27** crystal appear in P_1 and P_2 dimers, respectively, and thus, the highest hole and electron mobilities for **AQ27** both appear close to the P_1 and P_2 dimer direction, respectively. For the sake of discussions, the estimated two-dimensional anisotropic hole-transfer and electron-transfer mobilities of **AQ18**, **AQ23**, and **AQ27** in different molecular stacking layer are shown in Figures 8−. Figures 8a, 9a, and 10a depict the Cartesian coordinate system relative to the crystal axes' directions. From the predicted mobility anisotropic curve for compound **AQ18**, as shown in Figure 8, we determine that the $x-y$ plane is one of optimal conducting planes, and when the intersect angle between the transistor channel orientation and the x-axis (y-axis) direction approaches 30° (60°), the hole and electron mobility could achieve the highest values (0.11 and 0.25 $cm^2 \cdot V^{-1} \cdot s^{-1}$) at the same time. For compound **AQ27**, the $x-z$ plane is one of the optimal conducting planes, and when the intersect angle between the transistor channel orientation and the z-axis (x-axis) direction approaches 30° (60°), the hole and electron mobility could achieve the highest values (4.45 and 0.82 $cm^2 \cdot V^{-1} \cdot s^{-1}$) at the same time (see Figure 9). Different from **AQ18** and **AQ27** above, the maximum hole-transfer mobility (0.96 $cm^2 \cdot V^{-1} \cdot s^{-1}$) and electron-transfer mobility (0.32 $cm^2 \cdot V^{-1} \cdot s^{-1}$) of **AQ23** present at the z-axis and y-axis direction, respectively, and the optimal conducting plane is the crystal faces including z axis or y axis, as shown in Figure 10.

4. CONCLUSIONS

In conclusion, the electronic and charge transport properties of the derivatives of **AQ** have been investigated. Our results showed that (1) the electronic properties, reorganization energies, and intermolecular electronic couplings of **AQ** can be optimized by the regulation of substitution position and the number of substituents, which have significant influences on the frontier molecular orbital charge distributions and the steric hindrance and (2) from the view of electronic transport and electron injection, meta-substituted trifluoromethylethynyl groups are more beneficial to the improvement of OFET

https://doi.org/10.1021/acsomega.2c06591
ACS Omega 2022, 7, 48391−48402

properties of **AQ**. Furthermore, our simulations of angular resolution anisotropic mobility in 3D space and detailed analysis of the relationship between conducting channels and the crystal axis direction provide reference for the optimization OFET performance.

■ ASSOCIATED CONTENT

Supporting Information

The Supporting Information is available free of charge at https://pubs.acs.org/doi/10.1021/acsomega.2c06591.

The relative positions of the monomers in different dimers of studied compounds and frontier molecular orbitals' distribution in these dimers (PDF)

■ AUTHOR INFORMATION

Corresponding Author

Huipeng Ma − *College of Medical Laboratory Science, Dalian Medical University, Dalian 116044, China*; Email: huipeng_ma@126.com

Author

Jin-Dou Huang − *School of Physics and Materials Engineering, Dalian Nationalities University, Dalian 116600, China; State Key Laboratory of Molecular Reaction Dynamics, Dalian Institute of Chemical Physics, Chinese Academy of Sciences, Dalian 116023, China;* orcid.org/0000-0003-3747-9193

Complete contact information is available at: https://pubs.acs.org/10.1021/acsomega.2c06591

Notes

The authors declare no competing financial interest.

■ ACKNOWLEDGMENTS

This work was supported by the Educational Committee Foundation of Liaoning Province (grant LZ2020017) and the Program for Science and Technology Project of Liaoning Province (grants 2019-ZD-0188 and 2022-MS163). We gratefully acknowledge HZWTECH for providing computation facilities.

■ REFERENCES

(1) Kousseff, C. J.; Halaksa, R.; Parr, Z. S.; Nielsen, C. B. Mixed Ionic and Electronic Conduction in Small-Molecule Semiconductors. *Chem. Rev.* **2022**, *122*, 4397−4419.

(2) Pitsalidis, C.; Pappa, A.-M.; Boys, A. J.; Fu, Y.; Moysidou, C.-M.; van Niekerk, D.; Saez, J.; Savva, A.; Iandolo, D.; Owens, R. M. Organic Bioelectronics for In Vitro Systems. *Chem. Rev.* **2022**, *122*, 4700−4790.

(3) Feng, K.; Guo, H.; Sun, H.; Guo, X. n-Type Organic and Polymeric Semiconductors Based on Bithiophene Imide Derivatives. *Acc. Chem. Res.* **2021**, *54*, 3804−3817.

(4) Mola, G. T.; Ahmed, A. Y. A.; Ike, J. N.; Liu, M.; Hamed, M. S. G.; Zhang, Y. Engineering Non-fullerene Acceptors as a Mechanism to Control Film Morphology and Energy Loss in Organic Solar Cells. *Energy Fuels* **2022**, *36*, 4691−4707.

(5) Lin, Y.; Zhan, X. Oligomer Molecules for Efficient Organic Photovoltaics. *Acc. Chem. Res.* **2016**, *49*, 175−183.

(6) Kumagai, S.; Ishii, H.; Watanabe, G.; Yu, C. P.; Watanabe, S.; Takeya, J.; Okamoto, T. Nitrogen-Containing Perylene Diimides: Molecular Design, Robust Aggregated Structures, and Advances in n-Type Organic Semiconductors. *Acc. Chem. Res.* **2022**, *55*, 660−672.

(7) Ma, X.; Jiang, Z.; Xiang, L.; Zhang, F. Natural Material Inspired Organic Thin-Film Transistors for Biosensing: Properties and Applications. *ACS Mater. Lett.* **2022**, *4*, 918−937.

(8) Koklu, A.; Ohayon, D.; Wustoni, S.; Druet, V.; Saleh, A.; Inal, S. Organic Bioelectronic Devices for Metabolite Sensing. *Chem. Rev.* **2022**, *122*, 4581−4635.

(9) McCuskey, S. R.; Chatsirisupachai, J.; Zeglio, E.; Parlak, O.; Panoy, P.; Herland, A.; Bazan, G. C.; Nguyen, T.-Q. Current Progress of Interfacing Organic Semiconducting Materials with Bacteria. *Chem. Rev.* **2022**, *122*, 4791−4825.

(10) Anthony, J. E.; Facchetti, A.; Heeney, M.; Marder, S. R.; Zhan, X. n-Type Organic Semiconductors in Organic Electronics. *Adv. Mater.* **2010**, *22*, 3876−3892.

(11) Usta, H.; Kim, D.; Ozdemir, R.; Zorlu, Y.; Kim, S.; Ruiz Delgado, M. C.; Harbuzaru, A.; Kim, S.; Demirel, G.; Hong, J.; Ha, Y.-G.; Cho, K.; Facchetti, A.; Kim, M.-G. High Electron Mobility in [1]Benzothieno[3,2-b][1]benzothiophene-Based Field-Effect Transistors: Toward n-Type BTBTs. *Chem. Mater.* **2019**, *31*, 5254−5263.

(12) Zhao, M.; Yang, X.; Tsui, G. C.; Miao, Q. Trifluoromethylation of Anthraquinones for n-Type Organic Semiconductors in Field Effect Transistors. *J. Org. Chem.* **2020**, *85*, 44−51.

(13) Kim, C.; Facchetti, A.; Marks, T. J. Gate Dielectric Microstructural Control of Pentacene Film Growth Mode and Field-Effect Transistor Performance. *Adv. Mater.* **2007**, *19*, 2561−2566.

(14) Shuai, Z.; Wang, L.; Li, Q. Evaluation of Charge Mobility in Organic Materials: From Localized to Delocalized Descriptions at a First-Principles Level. *Adv. Mater.* **2011**, *23*, 1145−1153.

(15) Wang, L.; Nan, G.; Yang, X.; Peng, Q.; Li, Q.; Shuai, Z. Computational methods for design of organic materials with high charge mobility. *Chem. Soc. Rev.* **2010**, *39*, 423−434.

(16) Yang, X.; Wang, L.; Wang, C.; Long, W.; Shuai, Z. Influences of Crystal Structures and Molecular Sizes on the Charge Mobility of Organic Semiconductors: Oligothiophenes. *Chem. Mater.* **2008**, *20*, 3205−3211.

(17) Norton, J. E.; Brédas, J.-L. Polarization energies in oligoacene semiconductor crystals. *J. Am. Chem. Soc.* **2008**, *130*, 12377−12384.

(18) Yin, S.; Li, L.; Yang, Y.; Reimers, J. R. Challenges for the Accurate Simulation of Anisotropic Charge Mobilities through Organic Molecular Crystals: The beta Phase of mer-Tris(8-hydroxyquinolinato)aluminum(III) (Alq3) Crystal. *J. Phys. Chem. C* **2012**, *116*, 14826−14836.

(19) Zhao, Y.; Liang, W. Z. Charge transfer in organic molecules for solar cells: theoretical perspective. *Chem. Soc. Rev.* **2012**, *41*, 1075−1087.

(20) Marcus, R. A. Electron transfer reactions in chemistry. Theory and experiment. *Rev. Mod. Phys.* **1993**, *65*, 599−610.

(21) Lin, S. H., Chang, C. H., Liang, K. K., Chang, R., Shiu, Y. J., Zhang, J. M., Yang, T. S., Hayashi, M., Hsu, F. C., *Ultrafast Dynamics and Spectroscopy of Bacterial Photosynthetic Reaction Centers Advances In Chemical Physics*; Wiley2002, *121*, 1−88.

(22) Reimers, J. R. A practical method for the use of curvilinear coordinates in calculations of normal-mode-projected displacements and Duschinsky rotation matrices for large molecules. *J. Chem. Phys.* **2001**, *115*, 9103.

(23) Lee, C.; Yang, W.; Parr, R. G. Development of the Colle-Salvetti correlation-energy formula into a functional of the electron density. *Phys. Rev. B* **1988**, *37*, 785.

(24) Valeev, E. F.; Coropceanu, V.; da Silva Filho, D. A.; Salman, S.; Brédas, J.-L. Effect of Electronic Polarization on Charge-Transport Parameters in Molecular Organic Semiconductors. *J. Am. Chem. Soc.* **2006**, *128*, 9882−9886.

https://doi.org/10.1021/acsomega.2c06591
ACS Omega 2022, 7, 48391−48402